The Dynamics of the Onset of Frictional Slip

Oded Ben-David, *et al.*

Science **330**, 211 (2010);
DOI: 10.1126/science.1194777

This copy is for your personal, non-commercial use only.

If you wish to distribute this article to others, you can order high-quality copies for your colleagues, clients, or customers by clicking here.

Permission to republish or repurpose articles or portions of articles can be obtained by following the guidelines here.

The following resources related to this article are available online at www.sciencemag.org (this infomation is current as of April 5, 2011):

Updated information and services, including high-resolution figures, can be found in the online version of this article at:
http://www.sciencemag.org/content/330/6001/211.full.html

Supporting Online Material can be found at:
http://www.sciencemag.org/content/suppl/2010/10/05/330.6001.211.DC1.html

A list of selected additional articles on the Science Web sites **related to this article** can be found at:
http://www.sciencemag.org/content/330/6001/211.full.html#related

This article **cites 25 articles**, 3 of which can be accessed free:
http://www.sciencemag.org/content/330/6001/211.full.html#ref-list-1

This article has been **cited by** 1 articles hosted by HighWire Press; see:
http://www.sciencemag.org/content/330/6001/211.full.html#related-urls

This article appears in the following **subject collections:**
Geochemistry, Geophysics
http://www.sciencemag.org/cgi/collection/geochem_phys

Science (print ISSN 0036-8075; online ISSN 1095-9203) is published weekly, except the last week in December, by the American Association for the Advancement of Science, 1200 New York Avenue NW, Washington, DC 20005. Copyright 2010 by the American Association for the Advancement of Science; all rights reserved. The title *Science* is a registered trademark of AAAS.

this location suggests extensive biodegradation, and comparison of methane oxidation rates to CH_4/C_2H_6 for all rate measurements reveals a positive exponential correlation (Fig. 4B). We interpret this relationship to reflect a slower substrate response and growth rate for methanotrophs relative to ethane degraders in the plume, although direct inhibition cannot be excluded. We suggest that the development of methanotrophic communities in deep hydrocarbon plumes is delayed with respect to that of ethane-, propane-, and butane-consuming communities.

To identify potential propane- and ethane-consuming bacteria active in the deep plumes, we collected cells and sequenced bacterial DNA from five locations containing distinctive propane and ethane anomalies. A cloning-based survey of the 16*S* rRNA gene was dominated by several sequences related to known hydrocarbon degraders—*Cycloclasticus* (*21*–*24*), *Colwellia* (*25*), and members of the *Oceanospirillaceae* (*26*)—indicating a low diversity bloom of hydrocarbon-oxidizing bacteria in the deep plumes. The plume closest to the wellhead had the highest levels of hydrocarbons and the least evidence for biodegradation and yielded the lowest proportion of putative hydrocarbon degraders (52%) relative to typical mesopelagic bacteria. We take this location to represent an early developmental stage in the bloom of hydrocarbon-oxidizing bacteria. The remaining four locations were each dominated by two clades of putative hydrocarbon degraders (Fig. 3B) related to *Cycloclasticus* and *Colwellia*, contrasting previous results (*16*) that found relatives of the *Oceanospirillaceae* as the dominant phylotypes. We suggest that the observed relatives of *Cycloclasticus* and/or *Colwellia* are blooming as a result of their capacity to consume propane, ethane, and potentially butane, although not at the exclusion of other bacteria or metabolisms. While *Cycloclasticus* is known for its ability to degrade aromatic compounds, sequences observed here are 90% similar to putative ethane and propane oxidizers identified by stable isotope probing (*27*), indicating the capability in this evolutionary lineage (Fig. 3C).

The extent to which various hydrocarbons may feed respiration and bacterial blooms depends on their concentration and bioavailability. Based on several assumptions (*6*), we calculate that methane, ethane, and propane released from the Deepwater Horizon leak will exert a biological oxygen demand in the deep plume horizon of up to 8.3×10^{11} g O_2 for methane respiration, 1.3×10^{11} g O_2 for ethane, and 1.0×10^{11} g O_2 for propane. In comparison, assuming that 968,000 barrels of oil were dispersed into the subsurface (*5*, *6*), we calculate a maximum biological oxygen demand for oil of 4.4×10^{11} g O_2. The sum of these values, $\sim 1.5 \times 10^{12}$ g of O_2, provides an estimate of the maximum integrated deep-water O_2 anomaly expected from this event, with roughly 15% of the oxygen loss occurring in fresh plumes from respiration of propane and ethane. From these estimates, we predict that roughly two-thirds of the ultimate microbial productivity in deep plumes will arise from metabolism of natural gas. We also predict boom-and-bust cycles of bacterial succession beginning with propane, ethane, and butane consumers, followed by the consumers of various higher hydrocarbons and methane. However, the plumes' bacterial population will also respond to persistent mixing of bacteria, oxygen, and hydrocarbons with nonplume waters, which could presumably lead to attenuation in the aging plumes.

References and Notes

1. L. K. Dasanayaka, P. D. Yapa, *J. Hydroenviron. Res.* **2**, 243 (2009).
2. P. D. Yapa, L. K. Dasanayaka, U. C. Bandara, K. Nakata, *Oceans* **1–4**, 109 (2008).
3. R. Camilli *et al.*, *Science* **330**, 201 (2010); published online 19 August 2010 (10.1126/science.1195223).
4. F. Chen, P. D. Yapa, *J. Mar. Syst.* **45**, 189 (2004).
5. U.S. Geological Survey, "Deepwater Horizon MC252 Gulf Incident Oil Budget: Government Estimates - Through August 01 (Day 104)" (USGS, 2010); www.noaanews.noaa.gov/stories2010/PDFs/DeepwaterHorizonOilBudget20100801.pdf.
6. Materials and methods are available on *Science* Online.
7. D. Valentine, *Nature* **465**, 421 (2010).
8. J. M. Brooks, thesis, Texas A&M University (1975).
9. N. J. Grant, M. J. Whiticar, *Global Biogeochem. Cycles* **16**, 1124 (2002).
10. S. Mau *et al.*, *Mar. Geol.* **225**, 129 (2006).
11. S. Mau *et al.*, *Geophys. Res. Lett.* **34**, L22603 (2007).
12. W. S. Reeburgh, *Chem. Rev.* **107**, 486 (2007).
13. D. L. Valentine, D. C. Blanton, W. S. Reeburgh, M. Kastner, *Geochim. Cosmochim. Acta* **65**, 2633 (2001).
14. M. Schrope, *Nature* **465**, 274 (2010).
15. Joint Analysis Group, "Review of Preliminary Data to Examine Subsurface Oil in the Vicinity of MC252#1 May 19 to June 19, 2010" (NOAA, 2010); http://beta.w1.noaa.gov/sciencemissions/PDFs/JAG_Data_Report_Subsurface%20Oil_Final.pdf.
16. T. C. Hazen *et al.*, *Science* **330**, 204 (2010); published online 24 August 2010 (10.1126/science.1195979).
17. F. S. Kinnaman, D. L. Valentine, S. C. Tyler, *Geochim. Cosmochim. Acta* **71**, 271 (2007).
18. J. T. Gelwicks, J. B. Risatti, J. M. Hayes, *Org. Geochem.* **14**, 441 (1989).
19. J. T. Gelwicks, J. B. Risatti, J. M. Hayes, *Appl. Environ. Microbiol.* **60**, 467 (1994).
20. V. Mastalerz, G. J. de Lange, A. Dahlmann, *Geochim. Cosmochim. Acta* **73**, 3849 (2009).
21. S. E. Dyksterhouse, J. P. Gray, R. P. Herwig, J. C. Lara, J. T. Staley, *Int. J. Syst. Bacteriol.* **45**, 116 (1995).
22. A. D. Geiselbrecht, B. P. Hedlund, M. A. Tichi, J. T. Staley, *Appl. Environ. Microbiol.* **64**, 4703 (1998).
23. A. Maruyama *et al.*, *Microb. Ecol.* **46**, 442 (2003).
24. W. K. Chung, G. M. King, *Appl. Environ. Microbiol.* **67**, 5585 (2001).
25. O. G. Brakstad, I. Nonstad, L. G. Faksness, P. J. Brandvik, *Microb. Ecol.* **55**, 540 (2008).
26. B. P. Hedlund, A. D. Geiselbrecht, T. J. Bair, J. T. Staley, *Appl. Environ. Microbiol.* **65**, 251 (1999).
27. M. C. Redmond, D. L. Valentine, A. L. Sessions, *Appl. Environ. Microbiol.*; published online 30 July 2010 (10.1128/AEM.00271-10).

28. This research was supported by the National Science Foundation through awards OCE 1042097 and OCE 0961725 to D.L.V. and OCE 1042650 and OCE 0849246 to J.D.K. and by the Department of Energy through award DE-NT0005667 to D.L.V. We thank the captain and crew of the research vessel *Cape Hatteras*, R. Stephens Smith, R. Amon, K. Goodman S. Bagby, G. Paradis, A. Best, L. Werra, C. Hansen, L. Sanchez, H. Hill, S. Joye, and the staff at Picarro Inc. for valuable technical assistance and discussions. Sequences are available on GenBank, accession numbers HQ222989 to HQ222996.

Supporting Online Material

www.sciencemag.org/cgi/content/full/science.1196830/DC1
Materials and Methods
Figs. S1 to S6
Table S1
References

23 August 2010; accepted 8 September 2010
Published online 16 September 2010;
10.1126/science.1196830
Include this information when citing this paper.

The Dynamics of the Onset of Frictional Slip

Oded Ben-David, Gil Cohen, Jay Fineberg*

The way in which a frictional interface fails is critical to our fundamental understanding of failure processes in fields ranging from engineering to the study of earthquakes. Frictional motion is initiated by rupture fronts that propagate within the thin interface that separates two sheared bodies. By measuring the shear and normal stresses along the interface, together with the subsequent rapid real-contact-area dynamics, we find that the ratio of shear stress to normal stress can locally far exceed the static-friction coefficient without precipitating slip. Moreover, different modes of rupture selected by the system correspond to distinct regimes of the local stress ratio. These results indicate the key role of nonuniformity to frictional stability and dynamics with implications for the prediction, selection, and arrest of different modes of earthquakes.

The relative motion of two contacting bodies under an imposed shear is governed by the ensemble of discrete contacts composing their interface (*1*). Although frictional slip (*2*, *3*) is initiated by the rapid rupture of these contacts, understanding of the mechanisms of how interface rupture takes place is limited by our knowledge of the properties, strength, and stability of this rough interface.

Frontlike rupture modes bridge the gap between the microscopic interactions that define local frictional resistance and the resulting macroscopic motion imbued in the slip of large bodies

---

Racah Institute of Physics, the Hebrew University of Jerusalem, Givat Ram, Jerusalem, Israel.

*To whom correspondence should be addressed. E-mail: jay@vms.huji.ac.il

(*2*–*4*). Laboratory experiments reveal three distinct modes of rupture: (i) slow ruptures, which propagate far below material wave speeds (*5*–*8*), (ii) "sub-Rayleigh" ruptures (*5*, *6*, *9*–*12*) that propagate up to the Rayleigh wave speed, and (iii) "supershear" rupture modes that surpass the shear wave speed C_S (*5*, *10*, *12*). Sub-Rayleigh ruptures are related to shear fracture, which is well understood theoretically (*2*); however, our understanding of the other rupture modes is much less clear. Supershear modes, which have long been considered theoretically possible in shear fracture (*13*–*16*), have only recently been observed (*12*), whereas our understanding of slow rupture modes is still very much in its infancy (*17*, *18*). Each of these rupture modes may occur in earthquakes, but if, where, and how they are selected are still open questions. Although sub-Rayleigh modes are considered the most general mode of earthquake propagation (*2*, *4*, *15*), there is mounting evidence for the importance of both slow (*19*–*21*) and supershear (*22*, *23*) rupture modes along natural faults.

To understand how properties of frictional rupture couple to the profiles of local stresses along a frictional interface, we conducted experiments with acrylic poly(methyl-methacrylate) blocks in two qualitatively different loading systems (fig. S1) (*24*). At the start of each experiment, the blocks were pressed together by a normal force F_N (Fig. 1A). External shear forces, F_S, were applied to either the trailing edge ($x = 0$) of the top-block, uniformly along the bottom block, or in a mixture of the two. F_S was incremented quasi-statically, eventually triggering stick-slip sliding. We continuously performed simultaneous measurements of the real contact area, $A(x,t)$, at every point x at rates of up to 250,000 samples/s (here, t is time). In parallel, shear and normal stress profiles adjacent to the interface, $\tau(x)$ and $\sigma(x)$, respectively, were measured every second. All rupture events encompassing either partial sections of the interface (*6*) or the entire interface were measured.

In nearly all frictional systems, $\tau(x)$ and $\sigma(x)$ are highly nonuniform, suggesting that nonuniformity is generic. Even in ideal laboratory systems, large stress nonuniformity can be produced by minute interface curvature, differences in the materials and/or geometries of the contacting bodies, or dynamically, by earlier slip events (*6*, *17*). In the example presented in Fig. 1, B and C, we show how geometrically dissimilar blocks generate large shear stress variations at an optically flat interface under uniform application of F_N (Fig. 1). Because the dimensions of the upper and lower blocks are not identical, differential Poisson expansion is countered by pinning of the blocks at the frictional interface (*25*). This generates shear stresses even for $F_S = 0$. Additional large stress variations result from any torque when $F_S > 0$ is applied.

Controlled variations of loading conditions (*24*) lead to spatial variations of $\tau(x)$ and $\sigma(x)$ that produced the full range of rupture modes (Fig. 2). These include individual events (Fig. 2, A to C) where slow, sub-Rayleigh, and supershear ruptures or combinations of these modes (Fig. 2A) took place. Additionally, the dynamics of rupture can change in successive events within a single stick-slip sequence (Fig. 2, D to F). All events in this sequence nucleated at approximately the same location ($x \sim 150$ mm) and propagated in both directions. In the first stick-slip event (Fig. 2D), the left-traveling front initiated at near-shear velocity, then continually slowed until ultimately arresting at $x \sim 50$ mm. In the second event, the left-traveling front initiated beyond the shear-wave speed (~1600 m/s), slowed to sub-Rayleigh propagation (250 to 500 m/s) near the sample edge, but did not arrest. The left-propagating front in the third event initiated at a super-shear velocity (~2300 m/s) and traversed the entire interface without slowing down. The rupture direction need not correspond to the resulting slip, which is determined by the loading.

Comparison of the rupture velocities to the local stress ratio, $\tau(x)/\sigma(x)$, suggests that this quantity is strongly coupled to the local front dynamics (Fig. 2). The local propagation speeds consistently increase with $\tau(x)/\sigma(x)$, with front arrest occurring when $\tau(x)/\sigma(x)$ falls below ~0.5 (for example, Fig. 2A at $x = 50$ mm). This qualitative dependence is both local along the interface and independent of how the local stress ratios were imposed. Supershear fronts can also nucleate under quasi-static external loading (Fig. 2, C and F). These ruptures can abruptly initiate (Fig. 2C), even when preceded by a slow, gradual nucleation process.

The local propagation velocities $V(x)$ of 287 different fronts as a function of $\tau(x)/\sigma(x)$, measured before slip initiation, demonstrate the generality of these observations (Fig. 3). Each front is part of a system-sized event, with each $V(x)$ indicating the instantaneous rupture velocity as a front traverses a specific strain gage. If we consider only fronts traversing locations far from the system's loading points or free edges, the data collapse onto a rough curve whose form indicates three distinct regimes of rupture dynamics: (i) slow fronts [$\tau(x)/\sigma(x) < 0.5$], (ii) sub-Rayleigh fronts [$0.5<\tau(x)/\sigma(x) < 0.8$], and (iii) supershear rupture [$\tau(x)/\sigma(x) > 0.8$]. The data collapse occurred for widely different external loading conditions (*24*), including simple edge-loading, a combination of uniform shear and edge loading, and uniform shear loading (compare with Figs. 1 and 2). This suggests that rupture-mode selection is coupled to $\tau(x)/\sigma(x)$, though it is not explicitly dependent on how loads are applied. The data fail to collapse in regions (for example, near loading points) where stress gradients are so large that stresses at the interface do not mirror those relieved in the local vicinity of the rupture tip.

At loading levels that are even incrementally below that needed to precipitate each slip event in Fig. 3, no slip occurred. Thus, the system was stable for values of $\tau(x)/\sigma(x)$ that far exceeded the static-friction coefficient (*26*) $\mu_S = F_S/F_N \sim 0.5$. This is surprising, as it is generally believed (*3*) that the value of μ_S is the criterion for stability to

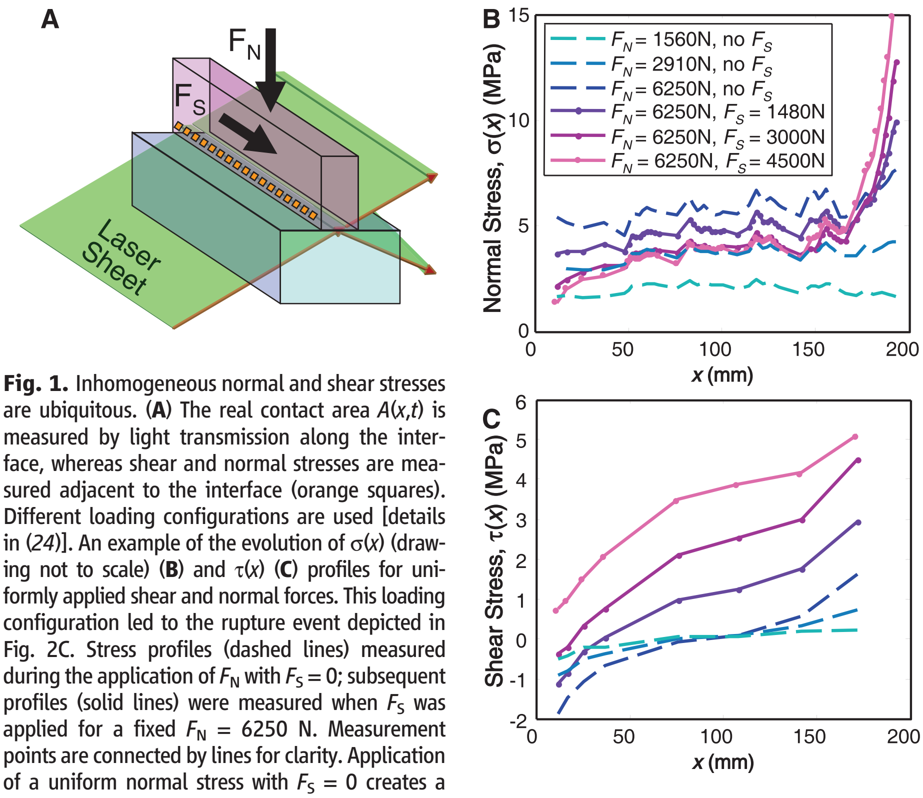

Fig. 1. Inhomogeneous normal and shear stresses are ubiquitous. (**A**) The real contact area $A(x,t)$ is measured by light transmission along the interface, whereas shear and normal stresses are measured adjacent to the interface (orange squares). Different loading configurations are used [details in (*24*)]. An example of the evolution of $\sigma(x)$ (drawing not to scale) (**B**) and $\tau(x)$ (**C**) profiles for uniformly applied shear and normal forces. This loading configuration led to the rupture event depicted in Fig. 2C. Stress profiles (dashed lines) measured during the application of F_N with $F_S = 0$; subsequent profiles (solid lines) were measured when F_S was applied for a fixed F_N = 6250 N. Measurement points are connected by lines for clarity. Application of a uniform normal stress with $F_S = 0$ creates a nonuniform antisymmetric $\tau(x)$ profile, solely as a result of differential Poisson expansion frustrated at the interface. Application of F_S increases the mean level of $\tau(x)$ while producing strong nonuniformity of $\sigma(x)$ near the block edges to compensate for external torque.

frictional motion at any point along a frictional interface. Our experiments demonstrate that this assumption is not valid; interfaces are locally stable even for local values of $\tau(x)/\sigma(x)$ that exceed $4\mu_S$ (Fig. 3). Although $\tau(x)/\sigma(x)$ can locally exceed μ_S, the integrated values of $\tau(x)$ and $\sigma(x)$ are consistent with the value of μ_S in each experiment.

When considering a frictional interface, it is tempting to simplify the problem by considering uniform stress profiles along the interface (*1*). Any geometrical or material mismatch, however, as well as the existence of edges, will lead to substantial nonuniformity (see, for example, Fig. 1). One can approximate uniform stress profiles only under a limited set of carefully controlled conditions (*12*, *26*). Thus, nonuniform stress profiles are the rule and are present on nearly any naturally occurring (*4*) or engineered frictional system. Along natural faults, heterogeneous profiles of $\sigma(x)$ or $\tau(x)$ can have a variety of additional origins. These include material heterogeneity of either shear strength or elastic moduli of the host material, inelastic deformations near fault tips, or spatial gradients of applied stress fields (*3*). Stress inhomogeneity can further evolve dynamically, through the partial release and transfer of stresses between slip patches (*2*, *4*, *15*) or by finite slip events driven by inhomogeneous stress application (*6*, *17*).

We can intuitively understand why the local stress ratio is tightly coupled to the rupture mode (*15*). We know that a crack propagates when the strain energy released in the bulk medium exceeds its fracture energy (*27*): the energy needed to create a new unit surface. At a frictional interface, this effective energy cost is proportional to the real area of contact $A(x)$, which is, in turn, locally proportional (*1*) to $\sigma(x)$ at each point x. Here, the effective fracture energy Γ is not a material-dependent quantity as in the fracture of bulk materials, but instead reflects the local strength of the interface, as determined by $\sigma(x)$. On the other hand, $\tau(x)$ is a locally measured quantity that mirrors the density of strain energy stored, before the arrival of a rupture front, within a region of finite size surrounding the point, x. Thus, at locations sufficiently removed from regions with high stress gradients, $\tau(x)/\sigma(x)$ reflects the balance between the potential energy available, before rupture, in the vicinity of each point and the energy needed to rupture the interface.

The idea of a material-dependent "peak" stress is frequently used to model material response at the tip of rapid ruptures (*2*, *16*, *28*). The peak stress, commonly denoted as τ_p, is often considered to be determined by the static-friction coefficient $\tau_p = \sigma(x) \cdot \mu_S$ (*3*). $\tau(x)$ can be considerably greater than this value (Fig. 3). Thus, if a characteristic τ_p exists, our peak results pose a lower limit for the peak strength and question the relevance of relating μ_S to local material strength.

Our results suggest that, once a rupture is nucleated, it will transition to supershear when a highly pre-stressed region is encountered. This is in agreement with numerically observed transitions to supershear rupture (*15*, *28*, *29*) in spa-

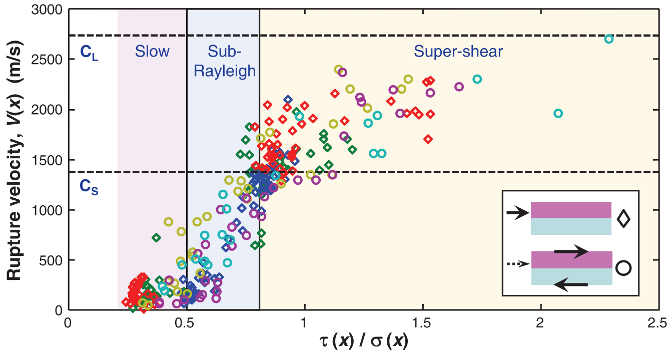

Fig. 3. Rupture-mode selection depends on $\tau(x)/\sigma(x)$. Local propagation velocities $V(x)$ as a function of $\tau(x)/\sigma(x)$ for 287 different fronts in system-sized slip events for edge-loading (diamonds) and (predominantly) uniformly applied shear (circles); see inset. The rough data collapse indicates three regimes in which $\tau(x)/\sigma(x)$ correlates well with the slow, sub-Rayleigh, and supershear rupture modes. Note that the local stress ratio $\tau(x)/\sigma(x)$ may far exceed the macroscopic static-friction coefficient $\mu_S \sim 0.5$. To avoid the effects of large stress gradients, all measurements were performed at strain-gage rosettes located away from sample edges at $x = 108$ mm (red), 142 mm (green), 172 mm (blue), 77 mm (magenta), 108 mm (yellow), and 142 mm (light blue). $V(x)$ was obtained from the contact area measurements surrounding these locations. Dashed lines indicate longitudinal (C_L) and shear (C_S) wave speeds.

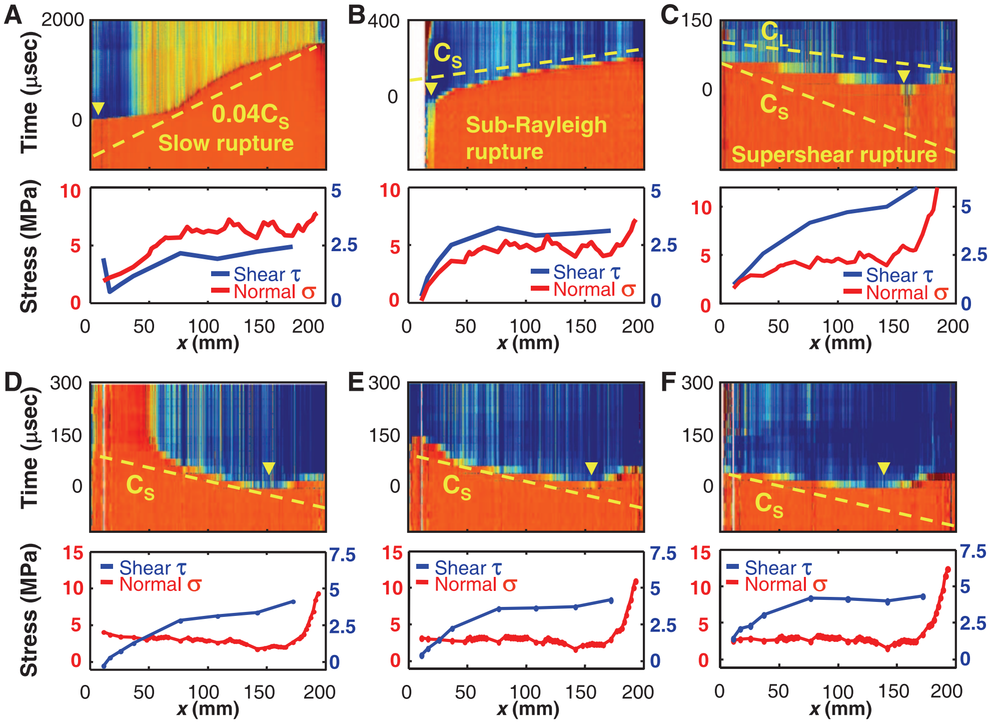

Fig. 2. Local stress profiles dramatically influence rupture dynamics. (Top panels) Changes in $A(x,t)$ normalized by $A(x,t = -1\text{ msec})$. Hotter (or colder) colors denote increased (or reduced, respectively) contact area. Rupture fronts are identified by a sharp change in color. Dashed lines denote sound speeds: $C_S = 1370$ m/s (shear) and $C_L = 2730$ m/s (longitudinal). (Bottom panels) Corresponding stress profiles before each event. Normal stress, $\sigma(x)$ (red lines), and shear stress, $\tau(x)$ (blue lines), are shown. Nucleation occurred at $t = 0$ at locations denoted by yellow arrowheads. (**A** to **C**) The three different rupture modes: slow (A), sub-Rayleigh (B), and super-shear (C). Events were generated in system II (*24*) where (A) the optional stopper was used, (B) the stopper was not used, or (C) the loading described in Fig. 1B was used. In (A) and (B), frustrated Poisson expansion was minimized by nonuniform application of $\sigma(x)$. (C) Note how the slow nucleation phase at $x \sim 150$ mm rapidly transitions to super-shear rupture. (**D** to **F**) Three successive slip events within the same stick-slip sequence as F_S was quasi-statically increased (loading conditions similar to Fig. 1). Events range from front arrest (D) to supershear rupture (F). Note that local stress ratios dramatically affect rupture dynamics: front arrest for $\tau(x)/\sigma(x) < 0.5$, slow rupture for $\tau(x)/\sigma(x) \sim 0.5$, sub-Rayleigh propagation for $\tau(x)/\sigma(x) \geq 0.5$, and super-shear rupture propagation where $\tau(x)/\sigma(x)$ is significantly larger than 0.5.

tially nonuniform systems when highly stressed regions are encountered; however, we do not yet fully understand what causes rupture nucleation in our system. We find that nucleation locations are often regions where $\tau(x)/\sigma(x)$ is maximal (for instance, see Fig. 2C). Hence, either low $\sigma(x)$ or high $\tau(x)$ can influence the location and initiation of rupture fronts. Increased $\sigma(x)$, as at the leading edge in Fig. 2F, will serve to suppress nucleation. Likewise, values of $\tau(x)$ that oppose the applied shear, such as at the trailing edges of Fig. 2, will have the same effect. The high values of both $\sigma(x)$ and $\tau(x)$ associated with corners can either make edges susceptible to rupture nucleation (Fig. 2A) or suppress rupture, depending on the competition between them.

Once a rupture front is nucleated, knowledge of the local stress profiles along the interface allows us to predict the rupture mode and could indicate when a rapid mode will either arrest to a complete stop (Fig. 2A) or evolve into a slow front (Fig. 2B). Thus, the initiation/transition locations of the slow fronts observed in previous studies (*5*, *6*) become clearer. Such questions of predictability are important when applied to understanding earthquake dynamics (*3*). Although $\tau(x)/\sigma(x)$ is an elusive quantity to measure along natural faults, indirect measurements may be possible by coupling precise measurements of spatial variations of $V(x)$ to laboratory measurements of the $\tau(x)/\sigma(x)$ dependence on V, as in Fig. 3. This estimate of this otherwise inaccessible quantity could provide some measure of predictability of the eventual size and dynamics of fast earthquakes along natural faults.

References and Notes

1. F. P. Bowden, D. Tabor, *The Friction and Lubrication of Solids* (Oxford Univ. Press, New York, ed. 2, 2001).
2. S. Das, *Pure Appl. Geophys.* **160**, 579 (2003).
3. C. H. Scholz, *The Mechanics of Earthquakes and Faulting* (Cambridge Univ. Press, Cambridge, ed. 2, 2002).
4. Y. Ben-Zion, *Rev. Geophys.* **46**, RG4006 (2008).
5. S. M. Rubinstein, G. Cohen, J. Fineberg, *Nature* **430**, 1005 (2004).
6. S. M. Rubinstein, G. Cohen, J. Fineberg, *Phys. Rev. Lett.* **98**, 226103 (2007).
7. M. Ohnaka, L. F. Shen, *J. Geophys. Res. Solid Earth* **104**, 817 (1999).
8. S. Nielsen, J. Taddeucci, S. Vinciguerra, *Geophys. J. Int.* **180**, 697 (2010).
9. P. G. Okubo, J. H. Dieterich, *J. Geophys. Res. Solid Earth* **89**, 5817 (1984).
10. T. L. Johnson, C. H. Scholz, *J. Geophys. Res.* **81**, 881 (1976).
11. O. Ben-David, S. M. Rubinstein, J. Fineberg, *Nature* **463**, 76 (2010).
12. K. W. Xia, A. J. Rosakis, H. Kanamori, *Science* **303**, 1859 (2004).
13. S. Das, K. Aki, *Geophys. J. R. Astron. Soc.* **50**, 643 (1977).
14. R. Burridge, *Geophys. J. R. Astron. Soc.* **35**, 439 (1973).
15. R. Madariaga, K. B. Olsen, *Pure Appl. Geophys.* **157**, 1981 (2000).
16. D. J. Andrews, *J. Geophys. Res. Solid Earth* **81**, 5679 (1976).
17. O. M. Braun, I. Barel, M. Urbakh, *Phys. Rev. Lett.* **103**, 194301 (2009).
18. Y. J. Liu, J. R. Rice, *J. Geophys. Res. Solid Earth* **110**, B08307 (2005).
19. Y. Ito, K. Obara, K. Shiomi, S. Sekine, H. Hirose, *Science* **315**, 503 (2007); published online 30 November 2006 (10.1126/science.1134454).
20. A. T. Linde, M. T. Gladwin, M. J. S. Johnston, R. L. Gwyther, R. G. Bilham, *Nature* **383**, 65 (1996).
21. G. Rogers, H. Dragert, *Science* **300**, 1942 (2003); published online 8 May 2003 (10.1126/science.1084783).
22. R. J. Archuleta, *J. Geophys. Res. Solid Earth* **89**, 4559 (1984).
23. M. Bouchon, M. Vallée, *Science* **301**, 824 (2003).
24. Materials and methods are available as supporting material on *Science* Online.
25. S. M. Rubinstein, G. Cohen, J. Fineberg, *Phys. Rev. Lett.* **96**, 256103 (2006).
26. T. Baumberger, C. Caroli, *Adv. Phys.* **55**, 279 (2006).
27. L. B. Freund, *Dynamic Fracture Mechanics* (Cambridge Univ. Press, Cambridge, 1990).
28. E. M. Dunham, *J. Geophys. Res. Solid Earth* **112**, B07302 (2007).
29. Z. Q. Shi, Y. Ben-Zion, A. Needleman, *J. Mech. Phys. Solids* **56**, 5 (2008).

30. We thank E. Bouchbinder and A. Sagy for insightful comments and S. Kimhi for help with the system design. We acknowledge the support of grant 2006288 awarded by the U.S.-Israel Binational Science Foundation and the James S. McDonnell Foundation. We also acknowledge the European Science Foundation EUROCORES program FANAS for support via the Israel Science Foundation (grant 57/07). J.F. thanks the Max Born Chair for Natural Philosophy for support.

Supporting Online Material

www.sciencemag.org/cgi/content/full/330/6001/211/DC1
Materials and Methods
Fig. S1
References

7 July 2010; accepted 19 August 2010
10.1126/science.1194777

Block Copolymer Self-Assembly–Directed Single-Crystal Homo- and Heteroepitaxial Nanostructures

Hitesh Arora,[1,2]* Phong Du,[1]† Kwan W. Tan,[1] Jerome K. Hyun,[3]‡ John Grazul,[4] Huolin L. Xin,[3] David A. Muller,[5,6] Michael O. Thompson,[1] Ulrich Wiesner[1]§

Epitaxy is a widely used method to grow high-quality crystals. One of the key challenges in the field of inorganic solids is the development of epitaxial single-crystal nanostructures. We describe their formation from block copolymer self-assembly–directed nanoporous templates on single-crystal Si backfilled with Si or NiSi through a laser-induced transient melt process. Depending on thickness, template removal leaves either an array of nanopillars or porous nanostructures behind. For stoichiometric NiSi deposition, the template pores provide confinement, enabling heteroepitaxial growth. Irradiation through a mask provides access to hierarchically structured materials. These results on etchable and non-etchable materials suggest a general strategy for growing epitaxial single-crystal nanostructured thin films for fundamental studies and a wide variety of applications, including energy conversion and storage.

Most nanostructured inorganic materials directed by organic molecule self-assembly are either amorphous or polycrystalline (*1*–*7*). One of the key remaining issues in the field is the development of single-crystal nanostructured inorganic materials with an epitaxial relation to an underlying substrate. Such materials may enable advances in areas such as energy generation and storage. For example, the charge carrier mobility in crystalline materials in small dimensions is substantially reduced by grain boundaries, which decreases charge collection efficiency in photovoltaic cells (*8*). Although large-area patterned inorganic epitaxial single crystals have been synthesized before, the patterns have been limited to the micrometer scale (*9*). Several attempts have been made to achieve smaller-scale structures. Block copolymer thin films have been used as etching masks to generate inorganic nanostructures, but the process depends on etchable substrates, and the features can only be vertically aligned and are always open from the top (*10*–*13*). Laser-induced melting of Si and subsequent infiltration into a quartz mold have been previously described (*14*). The process relies on so-called top-down lithography and etching to make a mold, however, with a structural period of hundreds of nanometers. Moreover, the epitaxial relation of the resulting structures to the substrate was not elucidated, and the heteroepitaxy of non-etchable materials was not addressed. Directional rapid solidification and epitaxy have been described for semicrystalline block copolymer films, but without any inorganic materials (*15*). Hierarchically ordered oxide structures have been demonstrated before, but the oxides were not single-crystalline (*16*). Mesoporous, single-crystalline,

---

[1]Department of Materials Science and Engineering, Cornell University, Ithaca, NY 14853, USA. [2]School of Chemical and Biomolecular Engineering, Cornell University, Ithaca, NY 14853, USA. [3]Department of Physics, Cornell University, Ithaca, NY 14853, USA. [4]Cornell Center for Materials Research, Cornell University, Ithaca, NY 14853, USA. [5]School of Applied and Engineering Physics, Cornell University, Ithaca, NY 14853, USA. [6]Kavli Institute at Cornell for Nanoscale Science, Cornell University, Ithaca, NY 14853, USA.

*Present address: Intel Corporation, Chandler, AZ 85226, USA.
†Present address: DuPont Chemical Company, Wilmington, DE 19880, USA.
‡Present address: Department of Materials Science and Engineering, Northwestern University, Evanston, IL 60208, USA.
§To whom correspondence should be addressed. E-mail: ubw1@cornell.edu